AIAA JOURNAL
Vol. 34, No. 6, June 1996

Stability of Gyroelastic Beams

K. Yamanaka,* G. R. Heppler,† and K. Huseyin‡
University of Waterloo, Waterloo, Ontario N2L 3G1, Canada

An idealized mathematical model of a linear elastic Bernoulli–Euler beam, in which each element of the beam has an infinitesimal quantity of stored angular momentum, is presented. This continuous distribution of angular momentum is termed gyricity. The governing equations of motion are derived when the system is subject to conservative external loads. It is shown that these systems can display both static instabilities (divergence) and dynamic instabilities (flutter), that the structure of the stability regions depends on the distribution of stiffness, and that gyric stabilization is sometimes possible.

I. Introduction

GYROSCOPIC systems have been studied widely,[1–7] often with particular reference to spacecraft.[8–10] Gyroscopic elements, such as control-moment gyros or momentum wheels, have been used to control satellites by either regulating the direction (or the angular rate of change of the direction) of the angular momentum vector or by regulating the magnitude of the angular momentum. Control-moment gyros use the first angular rate-of-change method, and momentum wheels use the magnitude adjustment method.

Control strategies that involve a large number of momentum wheels and/or control-moment gyros have been proposed for use in large flexible spacecraft for the purposes of attitude control and shape control. The presence of a very large number of discrete rotors presents a significant analytical challenge. In cases where there are relatively few rotors, they have been treated as individual elements in the analysis, but this manner of treatment soon leads to an unwieldy system of equations when a large number of rotors are to be considered. D'Eleuterio and Hughes[11–15] have put forward a very convenient and useful means of modeling elastic structures that have a large number of small spinning rotors by way of the concept of a gyroelastic continuum.

A gyroelastic continuum is a concept that imagines a body that has a continuous distribution of mass, stiffness, and angular momentum. The angular momentum distribution is assumed to be independent of the motion of the body, and it is further assumed that it can be separately specified without dependence on the mass distribution or the stiffness distribution. D'Eleuterio and Hughes[11] have termed the distributed angular momentum as stored angular momentum, or gyricity, and the latter term is used here.

The dynamics of continuous elastic gyroscopic systems have been studied by D'Eleuterio and Hughes[11–15] for the case where the gyricity distribution is constant in time, in terms of both magnitude and direction. The vibration frequencies and mode shapes were studied and a number of orthogonality conditions for the modes were obtained. Discrete gyroscopic systems also have been studied along the same lines.[1–4]

Damaren and D'Eleuterio[16–18] extended the original work of D'Eleuterio and Hughes to look at lightly damped gyric systems and also at control issues associated with gyricity distributions. Damaren and D'Eleuterio[18] considered the case of a gyricity distribution that had the characteristics of control-moment gyros where the direction of the distributed gyricity vector could vary, but not the magnitude.

The stability characteristics of these gyroelastic systems have not been examined and it is the purpose of this paper to present some results in that regard. We present a brief derivation of the governing equations, including the contribution of external conservative applied forces, for a gyroelastic beam in which the magnitude and the orientation of the gyricity distribution are fixed. Previous papers on gyroelastic systems[11–18] have assumed that the gyricity distribution goes to zero at the surface of the body. Here, we admit the possibility that the gyricity distribution has a nonzero value at the surface of the body and present, in addition to the governing equations, the boundary conditions for that case. This is followed by an examination of the stability properties of the system, and we demonstrate that both static and dynamic instabilities are possible as the parameters are varied.

II. Continuum with Gyricity

In this section, we outline the development of the governing equations for a linear elastic body that has an intrinsic distribution of angular momentum. This development is, to a large extent, a brief review of the work reported by D'Eleuterio[12] but includes a generalization of the boundary conditions. A continuous flexible body with a continuous distribution of angular momentum $\boldsymbol{h}$, which is assumed to be included in the body, is termed a gyroelastic body, and the distributed angular momentum is termed gyricity.[12] The gyricity distribution can be expressed as $\boldsymbol{h}(x, y, z)$. The possibility that $\boldsymbol{h}$ may be a function of time is explicitly excluded from consideration here. To formulate the equations of motion for a continuum with gyricity, Hamilton's principle can be employed.

The kinetic energy $\mathrm{d}T$ of an infinitesimal element of mass $\rho\,\mathrm{d}V$, including gyricity, is given by

$$\mathrm{d}T = \tfrac{1}{2}\left(\boldsymbol{v} + \boldsymbol{\omega}_h^{\times}\boldsymbol{r}_h\right)\cdot\left(\boldsymbol{v} + \boldsymbol{\omega}_h^{\times}\boldsymbol{r}_h\right)\rho\,\mathrm{d}V \tag{1}$$

where $\boldsymbol{v}$ represents the velocity components related to the translational motion, $\boldsymbol{r}_h$ is the position of the element with respect to the origin of the body fixed frame, $\boldsymbol{\omega}_h$ is the absolute angular velocity, ρ is the volume mass density of the body, and any matrix $\boldsymbol{a}^{\times}$ is the cross-product matrix defined according to the convention introduced by Hughes.[9] The superscript $\times$ is an indication that, for example, $\boldsymbol{a}^{\times}$ is a skew symmetric matrix of the form

$$\boldsymbol{a}^{\times} = \begin{bmatrix} 0 & -a_3 & a_2 \\ a_3 & 0 & -a_1 \\ -a_2 & a_1 & 0 \end{bmatrix} \tag{2}$$

which is based on the vector components $\boldsymbol{a} = [a_1, a_2, a_3]^T$. This notation is consistent with the notation used by D'Eleuterio and Hughes[16–18] and by Damaren and D'Eleuterio[11–15] in their original work in this area. The angular velocity $\boldsymbol{\omega}_h$ can be divided into two parts: $\boldsymbol{\omega}_b$ is the elastic rotation of the element, and $\boldsymbol{\omega}_s$ is the implicit angular velocity of the gyricity. Therefore, the angular velocity $\boldsymbol{\omega}_h$ can be expressed as

$$\boldsymbol{\omega}_h = \boldsymbol{\omega}_b + \boldsymbol{\omega}_s \tag{3}$$

Received July 20, 1994; revision received Oct. 31, 1995; accepted for publication Dec. 21, 1995.

*Research Associate, Systems Design Engineering.
†Associate Professor, Systems Design Engineering. Senior Member AIAA.
‡Professor, Systems Design Engineering.

Substitution of Eq. (3) into Eq. (1) and integration over the volume V of the body yields the total kinetic energy T of the system, which can be expressed as

$$T = \frac{1}{2}\int_V \boldsymbol{v}\cdot\boldsymbol{v}\rho\,dV + \int_V \boldsymbol{v}\cdot(\boldsymbol{\omega}_h^{\times}\boldsymbol{r}_h)\rho\,dV + \int_V (\boldsymbol{\omega}_b^{\times}\boldsymbol{r}_h)\cdot(\boldsymbol{\omega}_s^{\times}\boldsymbol{r}_h)\rho\,dV + \frac{1}{2}\int_V (\boldsymbol{\omega}_b^{\times}\boldsymbol{r}_h)\cdot(\boldsymbol{\omega}_b^{\times}\boldsymbol{r}_h)\rho\,dV + \frac{1}{2}\int_V (\boldsymbol{\omega}_s^{\times}\boldsymbol{r}_h)\cdot(\boldsymbol{\omega}_s^{\times}\boldsymbol{r}_h)\rho\,dV \tag{4}$$

Associated with the velocity field $\boldsymbol{v}$ is the displacement field $\boldsymbol{u}$ (i.e., $\dot{\boldsymbol{u}} = \boldsymbol{v}$). The elastic deflections give rise to elastic strains and rotations. The rotational displacement is

$$\boldsymbol{\beta} = \tfrac{1}{2}\nabla^{\times}\boldsymbol{u} \tag{5}$$

where ∇ is the gradient operator and $\nabla^{\times}\boldsymbol{u}$ is the curl of $\boldsymbol{u}$. The angular velocity $\boldsymbol{\omega}_b$ referred to the mass distribution, to first order, can be expressed as[12]

$$\boldsymbol{\omega}_b = \dot{\boldsymbol{\beta}} = \tfrac{1}{2}\nabla^{\times}\dot{\boldsymbol{u}} = \tfrac{1}{2}\nabla^{\times}\boldsymbol{v} \tag{6}$$

The second term in Eq. (4), which will yield terms involving the first moment of the mass, becomes zero for a suitable choice of coordinate axes. Then, without loss of generality, the total kinetic energy can be summarized by

$$\begin{aligned} T &= \left(\frac{1}{2}\int_V \boldsymbol{v}\cdot\boldsymbol{v}\rho\,dV + \int_V (\boldsymbol{\omega}_b^{\times}\boldsymbol{r}_h)\cdot(\boldsymbol{\omega}_s^{\times}\boldsymbol{r}_h)\rho\,dV\right) \\ &\quad + \frac{1}{2}\int_V \left[\left(\tfrac{1}{2}\nabla^{\times}\boldsymbol{v}\right)^{\times}\boldsymbol{r}_h\right]\cdot\left[\left(\tfrac{1}{2}\nabla^{\times}\boldsymbol{v}\right)^{\times}\boldsymbol{r}_h\right]\rho\,dV \\ &\quad + \frac{1}{2}\int_V (\boldsymbol{\omega}_s^{\times}\boldsymbol{r}_h)\cdot(\boldsymbol{\omega}_s^{\times}\boldsymbol{r}_h)\rho\,dV \\ &= \frac{1}{2}[\boldsymbol{v}\ \boldsymbol{\omega}_b]\cdot\mathcal{M}\cdot[\boldsymbol{v}\ \boldsymbol{\omega}_b] + \boldsymbol{\omega}_s\cdot\boldsymbol{I}_s\cdot\boldsymbol{\omega}_b + \frac{1}{2}\boldsymbol{\omega}_s\cdot\boldsymbol{I}_s\cdot\boldsymbol{\omega}_s \\ &= \frac{1}{2}[\boldsymbol{v}\ \boldsymbol{\omega}_b]\cdot\mathcal{M}\cdot[\boldsymbol{v}\ \boldsymbol{\omega}_b] + (\mathcal{H}\cdot\boldsymbol{\omega}_b + T_s) \end{aligned} \tag{7}$$

where we have introduced $\mathcal{H} = \boldsymbol{I}_s\cdot\boldsymbol{\omega}_s$ which is interpreted as the angular momentum resulting from the gyricity, and $T_s = \frac{1}{2}\boldsymbol{\omega}_s\cdot\boldsymbol{I}_s\cdot\boldsymbol{\omega}_s$, which is the kinetic energy resulting solely from the gyricity; $\mathcal{M}$ is the inertia operator of the system.

The first term of Eq. (7) results from the motion of the distributed mass, and the latter two terms result from the gyricity distribution. Therefore, the total kinetic energy T of the system is composed of two parts. The first part of the kinetic energy results from the distributed mass, which can be expressed as

$$T_1 = \int_V \frac{1}{2}\dot{\boldsymbol{w}}^T\boldsymbol{M}\dot{\boldsymbol{w}}\,dV \tag{8}$$

where $\dot{\boldsymbol{w}}$ denotes the velocity distribution and $\boldsymbol{w}$ denotes the displacement distribution, which includes both translational and angular displacements. The displacement components of the system can be given by

$$\boldsymbol{w} = \begin{bmatrix} u(x,y,z,t) \\ v(x,y,z,t) \\ w(x,y,z,t) \end{bmatrix} \tag{9}$$

The second part of the kinetic energy results from the gyricity distribution. We note that, to second order, the angular velocity $\boldsymbol{\omega}_b$ resulting from the gyricity can be expressed as[12]

$$\boldsymbol{\omega}_b = \left(\boldsymbol{I} - \tfrac{1}{2}\boldsymbol{\alpha}^{\times}\right)\dot{\boldsymbol{\alpha}} \tag{10}$$

where $\boldsymbol{\alpha}$ is the elastic rotational displacement resulting from the displacement $\boldsymbol{w}$ and is expressed by the relation

$$\boldsymbol{\alpha} = \tfrac{1}{2}\nabla^{\times}\boldsymbol{w} \tag{11}$$

The contribution to the kinetic energy of an infinitesimal element resulting from the gyricity is

$$dT_2 = \left[\boldsymbol{h}^T\left(\boldsymbol{I} - \tfrac{1}{2}\boldsymbol{\alpha}^{\times}\right)\dot{\boldsymbol{\alpha}} + T_s'\right]dV \tag{12}$$

where $\boldsymbol{h}$ and T_s' are the densities associated with the intrinsic angular momentum $\mathcal{H}$ and the kinetic energy T_s in Eq. (7). Then, the kinetic energy T_2, resulting from the gyricity becomes

$$\begin{aligned} T_2 &= \int_V \left(\boldsymbol{h}^T\dot{\boldsymbol{\alpha}} - \frac{1}{2}\boldsymbol{h}^T\boldsymbol{\alpha}^{\times}\dot{\boldsymbol{\alpha}}\right)dV + \int_V T_s'\,dV \\ &= \int_V \boldsymbol{h}^T\left(\frac{1}{2}\nabla^{\times}\dot{\boldsymbol{w}}\right) - \frac{1}{2}\boldsymbol{h}^T\left(\frac{1}{2}\nabla^{\times}\boldsymbol{w}\right)^{\times}\left(\frac{1}{2}\nabla^{\times}\dot{\boldsymbol{w}}\right)dV + T_s \\ &= \int_V \boldsymbol{h}^T\left(\frac{1}{2}\nabla^{\times}\dot{\boldsymbol{w}}\right) + \frac{1}{2}\left(\frac{1}{2}\nabla^{\times}\boldsymbol{w}\right)^T\boldsymbol{h}^{\times}\left(\frac{1}{2}\nabla^{\times}\dot{w}\right)dV + T_s \end{aligned} \tag{13}$$

The total potential energy V also consists of two parts. The first part is composed of the strain energy V_1 of the system resulting from deformation of the elastic body, and the second part is composed of the work potential V_2 ($V_2 = -$work) resulting from an external load $\boldsymbol{P}$. Here, for simplicity, we consider only conservative external loads. The strain energy V_1 of the system can be expressed as

$$V_1 = \frac{1}{2}\int_V \boldsymbol{\epsilon}^T\boldsymbol{D}\boldsymbol{\epsilon}\,dV \tag{14}$$

where $\boldsymbol{\epsilon}$ is the vector of strains and $\boldsymbol{D}$ is the constitutive matrix for the system. The specific form that both $\boldsymbol{\epsilon}$ and $\boldsymbol{D}$ take depends on the type of structural element that is being modeled, be it rod, beam, plate, or shell.

Because we are considering conservative forces only, it is convenient to adopt a convention that allows us to identify the specific force components in a manner similar to that for the stress components. Then, for a force P_{ij} acting on the face, which has the ith axis outward normal and which is directed in the jth direction, the force components acting on the body can be expressed in a matrix form such as

$$\boldsymbol{Q} = \begin{bmatrix} P_{XX} & P_{XY} & P_{XZ} \\ P_{YX} & P_{YY} & P_{YZ} \\ P_{ZX} & P_{ZY} & P_{ZZ} \end{bmatrix} \tag{15}$$

where the constant matrix $\boldsymbol{Q}$ is called an external-load matrix. Now, let us consider the potential energy resulting from the external load. The potential energy $dV_2 = -dW_2$ in an infinitesimal element dV ($= dx\,dy\,dz$) resulting from displacement $\boldsymbol{w}$ can be expressed as[19]

$$dV_2 = -\nabla^T\boldsymbol{Q}\boldsymbol{w}\,dV \tag{16}$$

Therefore, the potential V_2 resulting from the external load is obtained by integrating Eq. (16) over the volume of the material. Then, combining the kinetic and potential energies, the Lagrangian $\mathcal{L}$ of the system is

$$\mathcal{L} = \frac{1}{2}\int_V \left[\dot{\boldsymbol{w}}^T\boldsymbol{M}\dot{\boldsymbol{w}} + \boldsymbol{h}^T\nabla^{\times}\dot{\boldsymbol{w}} + \left(\frac{1}{2}\nabla^{\times}\boldsymbol{w}\right)^T\boldsymbol{h}^{\times}\left(\frac{1}{2}\nabla^{\times}\dot{\boldsymbol{w}}\right) - \boldsymbol{\epsilon}^T\boldsymbol{D}\boldsymbol{\epsilon} + 2\nabla^T\boldsymbol{Q}\boldsymbol{w}\right]dV + T_s \tag{17}$$

III. Beam with Gyricity

Let us consider, as the specific structural element of interest, a beam with a gyricity distribution. When we consider a one-dimensional distribution of the gyricity, say, in the z direction, which corresponds to the direction of the neutral axis of the beam, the gyricity distribution function $\boldsymbol{h}$ can be expressed as $\boldsymbol{h} = h(z)\hat{k}$, where $\hat{k}$ is the unit vector in the z direction. To formulate the equations of motion of the system, let us consider the illustration in Fig. 1. Let

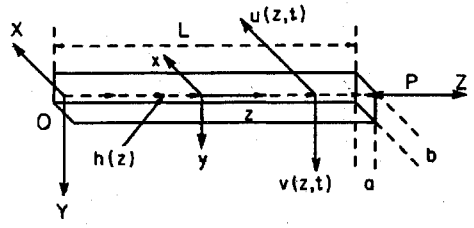

Fig. 1 Beam.

the $OXYZ$ axes be an inertial frame and the $Gxyz$ axes be a body fixed frame in which the point G is assumed to be on the neutral axis of the beam. One end of the beam is fixed at the origin of the inertial frame and the other end of the beam is free. The flexural stiffnesses of the beam are expressed by EI_{YY} and EI_{XX} in X and Y directions, respectively. The length of the beam is L, the cross-sectional area is A, and the volume mass density of the beam material is ρ. An external force acting at the tip of the beam, P, is assumed to remain parallel to the Z axis of the inertial frame. The displacements of the neutral axis of the beam in the X and Y directions, respectively, are $u(z)$ and $v(z)$. The axial displacement $w(z)$ of the beam is assumed to be negligible.

In terms of these parameters, the kinetic energy T_1 resulting from translational motion of the beam is expressed by

$$T_1 = \int_0^L \frac{1}{2}\rho A[(\dot{u})^2 + (\dot{v})^2]\,dz \tag{18}$$

The kinetic energy resulting from the gyricity distribution is given in Eq. (13). For the case at hand, and under the stated assumptions,

$$\boldsymbol{w} = \begin{bmatrix} u(z,t) \\ v(z,t) \\ -\left(x\dfrac{\partial u}{\partial z} + y\dfrac{\partial v}{\partial z}\right) \end{bmatrix} \quad \text{and} \quad \boldsymbol{h} = \begin{bmatrix} 0 \\ 0 \\ \hat{h}(z) \end{bmatrix} \tag{19}$$

By use of the above forms of $\boldsymbol{w}$ and $\boldsymbol{h}$, the kinetic energy T_2 is found to be

$$T_2 = \int_V \frac{1}{2}\hat{h}(z)(v'\dot{u}' - u'\dot{v}')\,dV \tag{20}$$

where $()'$ indicates differentiation with respect to z and $\dot{()}$ corresponds to differentiation with respect to time t. After integrating over $dA = dx\,dy$ and setting $\hat{h}(z)A = h(z)$, the gyroscopic contribution to the kinetic energy becomes

$$T_2 = \int_0^L \frac{1}{2}h(z)(v'\dot{u}' - u'\dot{v}')\,dz + T_s \tag{21}$$

The total potential energy resulting from the bending of the beam and the work of the conservative external load can be expressed as

$$V = \frac{1}{2}\int_0^L \left[EI_{YY}(u'')^2 + EI_{XX}(v'')^2\right]dz - \frac{1}{2}\int_0^L P[(u')^2 + (v')^2]\,dz \tag{22}$$

Here, for simplicity, both transverse shear and rotatory inertia of the beam are ignored. Then, the Lagrangian of the system can be written as

$$\mathcal{L} = \int_0^L \frac{1}{2}\rho A[(\dot{u})^2 + (\dot{v})^2] + \frac{1}{2}P\left[(u')^2 + (v')^2\right] - \frac{1}{2}\left[EI_{YY}(u'')^2 + EI_{XX}(v'')^2\right] + \frac{1}{2}h(z)(v'\dot{u}' - u'\dot{v}')\,dz + T_s \tag{23}$$

By applying Hamilton's principle to the above Lagrangian, the following relations can be obtained:

$$\delta\int_{t_1}^{t_2}\mathcal{L}\,dt = \int_{t_1}^{t_2}\int_0^L \rho A[\dot{u}\delta(\dot{u}) + \dot{v}\delta(\dot{v})] + P[u'\delta(u') + v'\delta(v')] - [EI_{YY}u''\delta(u'') + EI_{XX}v''\delta(v'')] + \frac{1}{2}h(z)[v'\delta(\dot{u}') - u'\delta(\dot{v}') + \dot{u}'\delta(v') - \dot{v}'\delta(u')]\,dz\,dt = 0 \tag{24}$$

By integrating by parts with respect to time only, the following variational equation can be obtained:

$$\Gamma_t + \int_{t_1}^{t_2}\int_0^L F(z)\,dz\,dt = 0 \tag{25}$$

where

$$\Gamma_t = \left\{\int_0^L \rho A[\dot{u}\delta(u) + \dot{v}\delta(v)] + \frac{1}{2}h(z)[v'\delta(u') + u'\delta(v')]\,dz\right\}_{t_1}^{t_2} \tag{26}$$

and

$$F(z) = -\rho A[\ddot{u}\delta(u) + \ddot{v}\delta(v)] + P[u'\delta(u') + v'\delta(v')] - [EI_{YY}u''\delta(u'') + EI_{XX}v''\delta(v'')] + h(z)[\dot{u}'\delta(v') - \dot{v}'\delta(u')] \tag{27}$$

Integrating $F(z)$ by parts leads to

$$\Gamma_z + \int_0^L G_u(z)\delta(u)\,dz + \int_0^L G_v(z)\delta(v)\,dz \tag{28}$$

where Γ_z are the boundary terms given by

$$\Gamma_z = [(Pu' - h(z)\dot{v}' + EI_{YY}u''')\delta(u)]_0^L - [(EI_{YY}u'')\delta(u')]_0^L + [(Pv' + h(z)\dot{u}' + EI_{XX}v''')\delta(v)]_0^L - [(EI_{XX}v'')\delta(v')]_0^L \tag{29}$$

and $G_u(z) = 0$ and $G_v(z) = 0$ are the Euler–Lagrange equations for the system. These are

$$\rho A\ddot{u} + EI_{YY}u'''' + Pu'' - \frac{d}{dz}[h(z)\dot{v}'] = 0 \tag{30}$$

and

$$\rho A\ddot{v} + EI_{XX}v'''' + Pv'' + \frac{d}{dz}[h(z)\dot{u}'] = 0 \tag{31}$$

The general solution can be obtained by taking the sum of the characteristic modes. However, it is apparent that the frequency equation and the mode shapes will be exceedingly complicated and hence very difficult to work with. Therefore, instead of obtaining the general solution, we seek an alternative approximate solution.

The trial functions for $u(z,t)$ and $v(z,t)$ were chosen to be of the form

$$u(z,t) = \sum_{m=1}^{N} A_m\phi_m(z)e^{j\omega t} \tag{32}$$

and

$$v(z,t) = \sum_{n=1}^{N} B_n\psi_n(z)e^{j\omega t} \tag{33}$$

where A_i and B_i are the undetermined parameters and $j = \sqrt{(-1)}$.

By substituting Eqs. (32) and (33) into Eq. (23) and taking the integral over space and time, and because the variations $\delta(\cdot)$ can now be considered with respect to the undetermined parameters, the following relation is obtained:

$$\int_{t_1}^{t_2} \sum_{m=1}^{N}\sum_{n=1}^{N} [A_m \quad B_m] \left\{ -\omega^2 \begin{bmatrix} -\rho A\int_0^L \phi_m\phi_n\,dz & 0 \\ 0 & -\rho A\int_0^L \psi_m\psi_n\,dz \end{bmatrix} + j\omega \begin{bmatrix} 0 & \int_0^L h(z)\phi_m'\psi_n'\,dz \\ -\int_0^L h(z)\psi_m'\phi_n'\,dz & 0 \end{bmatrix} \right.$$
$$\left. + \begin{bmatrix} P\int_0^L \phi_m'\phi_n'\,dz - EI_{YY}\int_0^L \phi_m''\phi_n''\,dz & 0 \\ 0 & P\int_0^L \psi_m'\psi_n'\,dz - EI_{XX}\int_0^L \psi_m''\psi_n''\,dz \end{bmatrix} \right\} \begin{bmatrix} \delta(A_n) \\ \delta(B_n) \end{bmatrix} dt = 0 \tag{34}$$

To proceed with the method of Ritz, the shape functions ϕ_m and ψ_m must be specified. The general mode shapes for a cantilever beam were chosen to be the basis functions that form the trial function. Hence, a basis function has the general form[20]

$$\Theta_n(z; c_n) = [\sin(c_n z) - \sinh(c_n z)] + \frac{\sin(c_n L) + \sinh(C_n L)}{\cos(c_n L) + \cosh(c_n L)}[\cos(c_n z) - \cosh(c_n z)] \tag{35}$$

where the frequency parameter

$$c_n = \left(\frac{\rho A\omega_n^2}{EI_{ii}}\right)^{\frac{1}{4}} \tag{36}$$

where $ii = YY$ or XX and n refers to the nth basis function. The frequency content of these shape functions is governed by the values of c_n. The values used in the following examples were obtained by using the roots of the frequency equation of a cantilever beam (with no gyricity) given by

$$1 + \cos(c_n L)\cosh(c_n L) = 0 \tag{37}$$

for any positive integer values n.

In the basis functions used to approximate $u(z, t)$, we replace c_m with $a_m[ii = YY$ in Eq. (36)]. In the basis functions used to approximate $v(z, t)$, we replace c_n with $b_n[ii = XX$ in Eq. (36)]. The basis functions for the u and v displacements then become $\phi_m(z) = \Theta_m(z; a_m)$ and $\psi_n(z) = \Theta_n(z; b_n)$, respectively.

A. One-Function Approximation

As an initial approximation, a one-term expansion, Eqs. (32) and (33), using the basis functions of the form of Eq. (35) was used with A_1 and B_1 as undetermined parameters.

Then, the variational equation in the matrix form can be expressed as

$$\int_{t_1}^{t_2} \Lambda_1^T \left[-\omega^2 \boldsymbol{M}_1 + j\omega \boldsymbol{G}_1 + \boldsymbol{K}_1\right] \delta\Lambda_1 e^{j2\omega t}\,dt = 0 \tag{38}$$

where $\boldsymbol{M}_1$, $\boldsymbol{G}_1$, and $\boldsymbol{K}_1$ can be deduced from Eq. (34) and $\Lambda_1^T = [A_1 \; B_1]$.[19] The stability properties of the system for the one-function approximation can be deduced from the characteristic equation

$$\Delta_1 = \det\left[-\omega^2 \boldsymbol{M}_1 + j\omega \boldsymbol{G}_1 + \boldsymbol{K}_1\right] = 0 \tag{39}$$

B. Two-Function Approximation

A more accurate approximate solution is possible by making use of more than one basis function for each of $u(z, t)$ and $v(z, t)$. By employing the two-function approximation [$N = 2$ in Eqs. (32) and (33)], a set of governing equations can be obtained in the form

$$\int_{t_1}^{t_2} \Lambda_2^T \left[-\omega^2 \boldsymbol{M}_2 + j\omega \boldsymbol{G}_2 + \boldsymbol{K}_2\right] \delta\Lambda_2 e^{j2\omega t}\,dt = 0 \tag{40}$$

where $\Lambda_2^T = [A_1 \; A_2 \; B_1 \; B_2]$ and $\boldsymbol{M}_2$, $\boldsymbol{G}_2$, and $\boldsymbol{K}_2$ are given in detail by Yamanaka.[19] The corresponding characteristic equation is obtained from

$$\Delta_2 = \det\left[-\omega^2 \boldsymbol{M}_2 + j\omega \boldsymbol{G}_2 + \boldsymbol{K}_2\right] = 0 \tag{41}$$

It can be shown that Δ_1 and Δ_2 contain only even powers of ω, so that it is expedient to make the substitution $\Omega = \omega^2$ and, for simplicity, in the remainder of this paper Ω is referred to as the frequency.

C. Stability Analysis of the Beam with Gyricity

1. *Example 1: One-Function Approximation for a Rectangular Beam*

To illustrate the stability analysis, we consider the case of a beam that has different bending stiffnesses in the x and y directions; this situation is referred to as a rectangular beam. The beam properties were chosen to correspond to a 1-m-long aluminum beam with a rectangular cross section that measured 1 × 2 cm. The associated parameter values are given in Table 1. The distribution of the angular momentum $h(z)$ is assumed to be constant, and an external conservative force P is applied at the tip of the beam. The characteristic equation for the rectangular beam is[21]

$$\Delta_1 = m_1 m_2 \Omega^2 - \left[g^2\xi + m_1(k_2 - Pf_2) + m_2(k_1 - Pf_1)\right]\Omega + (k_1 - Pf_1)(k_2 - Pf_2) = 0 \tag{42}$$

where

$$m_1 = \int_0^L \rho A\phi_1^2\,dz, \qquad m_2 = \int_0^L \rho A\psi_1^2\,dz \tag{43}$$

$$g = \int_0^L \phi_1'(z)\psi_1'(z)\,dz \tag{44}$$

$$k_1 = EI_{YY}\int_0^L (\phi_1'')^2\,dz, \qquad k_2 = EI_{XX}\int_0^L (\psi_1'')^2\,dz \tag{45}$$

$$f_1 = \int_0^L (\phi_1')^2\,dz, \quad \text{and} \quad f_2 = \int_0^L (\psi_1')^2\,dz \tag{46}$$

For notational convenience, we have introduced ξ such that $h = \text{constant} = \xi^{1/2}$. The divergence boundaries are two distinct vertical lines in the P–ξ plane, and they are given by

$$k_1 - Pf_1 = 0 \quad \text{and} \quad k_2 - Pf_2 = 0 \tag{47}$$

In the event that the beam has a square cross section (i.e., equal bending stiffness in the x and y directions) then $k_1 = k_2$ and $f_1 = f_2$ [noting that, in that case, $\phi_1(z) = \psi_1(z)$] and the divergence boundaries coalesce into a pair of coincident vertical lines.

The flutter boundaries are determined by the two relations

$$\Delta(\Omega) = 0 \quad \text{and} \quad \frac{\partial\Delta(\Omega)}{\partial\Omega} = 0 \tag{48}$$

Table 1 Parameters for the examples

Parameter	Values: Square	Values: Rectangular	Unit
EI_{XX}	57.5	115	$N \cdot m^2$
EI_{YY}	57.5	460	$N \cdot m^2$
M	0.276	0.552	kg
L	1.00	1.00	m
ρ	2.76×10^3	2.76×10^3	kg/m^3
A	1.00×10^{-4}	2.00×10^{-4}	m^2

which lead to

$$\zeta_{1,2} = (1/g^2)\Big\{[m_1(Pf_2 - k_2) + m_2(Pf_1 - k_1)] \pm 2[m_1 m_2 (Pf_1 - k_1)(Pf_2 - k_2)]^{\frac{1}{2}}\Big\} \tag{49}$$

which is the equation of a hyperbola. The general expressions for the center and asymptotes of the hyperbola can be found from Eq. (49), but for our choice of trial functions these parameters have particularly simple forms. The center is located at

$$\xi = 0 \qquad P = \tfrac{1}{2}(k_1 + k_2) \tag{50}$$

and the asymptotes are

$$\xi = 0 \qquad \xi = (1/g^2)[m_1(Pf_2 - k_2) + m_2(Pf_1 - k_1)] \tag{51}$$

where, in Eqs. (50) and (51), $m_1 = m_2 = m$, $f_1 = f_2 = f$ and $k = (k_2 + k_1)/2$.

In the case of a square beam where $k_1 = k_2$, the flutter boundaries degenerate from a hyperbola to a pair of straight lines given by

$$\xi = 0 \quad \text{and} \quad \xi = \frac{4m(Pf - k)}{g^2} \tag{52}$$

Note the similarity between the equations for the asymptotes of the hyperbola and the equations that define the flutter boundary for the square beam.

The stability boundary plot in the P–ξ plane for the case corresponding to the values in Table 1 is illustrated in Fig. 2, where S and F indicate stability and instability by flutter, respectively, and D and DD indicate instability by single and double divergence, respectively. The divergence boundaries, which correspond to the Euler buckling loads for the two principal directions, appear as the two vertical lines given by $P_{d_1} \simeq 305.9$ N and $P_{d_2} \simeq 1224$ N. For comparison, the corresponding exact values for the divergence boundaries (Euler buckling loads) are given by Timoshenko and Gere[22] as $P^*_{d_1} \simeq 283.8$ N and $P^*_{d_2} \simeq 1135$ N.

Some representative characteristic curves in the frequency Ω–ξ plane, for fixed values of the applied force P, are plotted in Fig. 3. For $P < P_{d_1}$ (represented by $P = 0$ in Fig. 3), the frequencies Ω remain positive for all values of ξ, indicating that the system is stable regardless of the value of ξ. In the case of loads on the interval corresponding to $P_{d_1} < P < P_{d_2}$ ($P = 1000$ in Fig. 3), the frequencies consist of one positive value and one negative value for all values of ξ. The persistent negative root means that the system is unstable by divergence regardless of the value of ξ. When $P > P_{d_2}$ ($P = 2000$ in Fig. 3), it can be observed that there is differing behavior of the roots, depending on the value of ξ. If $0 \le \xi \le \xi_d$ (i.e., for low values of ξ), the frequencies consist of two negative values, indicating instability by double divergence. This behavior is marked as region DD in Fig. 2. Higher values of ξ, those corresponding to the range $\xi_d < \xi < \xi_f$, cause the frequencies to consist of a pair of complex conjugates, thus indicating instability by flutter (region F in Fig. 2). As ξ is increased through the threshold value (flutter value) ξ_f, the system enters into a stable region where $\xi \ge \xi_f$. For these values of ξ there are two positive roots: Ω_1 and Ω_2. The stability in this part of the parameter plane results from the effect of the gyroscopic forces. The above observations have led to designating region S as stable, region D as unstable by divergence, region F as unstable by flutter, and region DD as unstable by double divergence in Fig. 2.

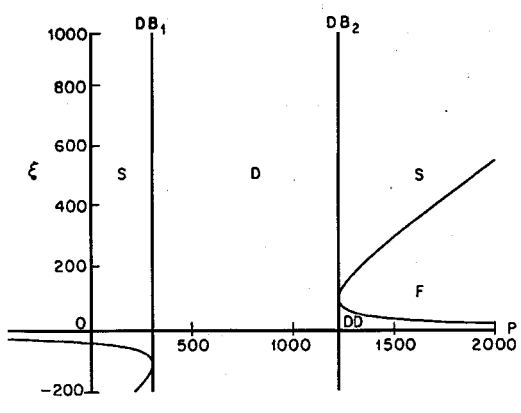

Fig. 2 Stability boundaries for the rectangular beam with gyricity by a one-function approximation.

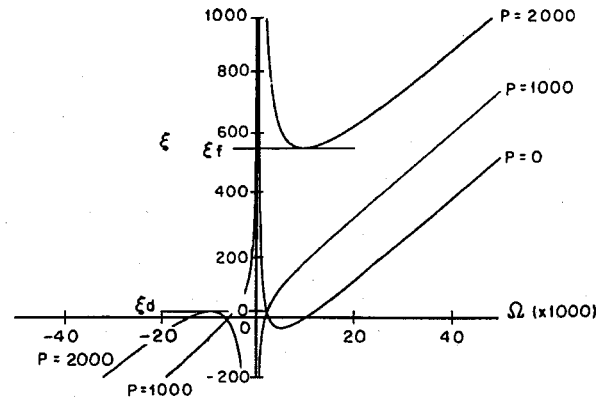

Fig. 3 Characteristic curves for the rectangular beam with gyricity by a one-function approximation at $P = 0$, 1000, and 2000 N.

2. Example 2: Two-Function Approximation for a Square Beam

In this example, by using two basis functions in the trial function, we investigate how the inclusion of more degrees of freedom in the Ritz approximation influences the stability behavior of a square beam. The beam parameters are given in Table 1.

The characteristic equation $\Delta_2 = 0$ is of the form

$$\Delta_2 = \mathcal{P}_4\Omega^4 + \mathcal{P}_3(P, \xi)\Omega^3 + \mathcal{P}_2(P^2, P, \xi P, \xi^2, \xi)\Omega^2 + \mathcal{P}_1(P^3, P^2, P, \xi P^2, \xi P, \xi)\Omega + \mathcal{P}_0(P^4, P^3, P^2, P) = 0 \tag{53}$$

The details of the $\mathcal{P}_i$ are too long to be included here, but it is useful to know that

$$\mathcal{P}_4 = (m_{11}m_{22} - m_{12}^2)^2 \tag{54}$$

is always positive and only depends on the indicated entries in the mass matrix (for the square beam, note that $m_{11} = m_{33}$, $m_{22} = m_{44}$, $m_{12} = m_{34}$).

The divergence boundaries are two vertical lines in the P–ξ plane, and the values of P that correspond to these boundaries can be shown to satisfy $\mathcal{P}_0 = 0$ or

$$[(f_{11}f_{22} - f_{12}^2)P^2 - (f_{11}k_{22} + f_{22}k_{11} - 2f_{12}k_{12})P + (k_{11}k_{22} - k_{12}^2)]^2 = 0 \tag{55}$$

which has two pairs of repeated roots. The parameters f_{ij}, k_{ij} are given by

$$f_{11} = \int_0^L (\phi_1')^2\,dz == \int_0^L (\psi_1')^2\,dz = f_{33} \tag{56}$$

$$f_{12} = f_{21} = \int_0^L \phi_1'\phi_2'\,dz == \int_0^L \psi_1'\psi_2'\,dz = f_{34} = f_{43} \tag{57}$$

$$f_{22} = \int_0^L (\phi_2')^2\,dz == \int_0^L (\psi_2')^2\,dz = f_{44} \tag{58}$$

$$k_{11} = \int_0^L EI(\phi_1')^2\,dz == \int_0^L EI(\psi_1')^2\,dz = k_{33} \tag{59}$$

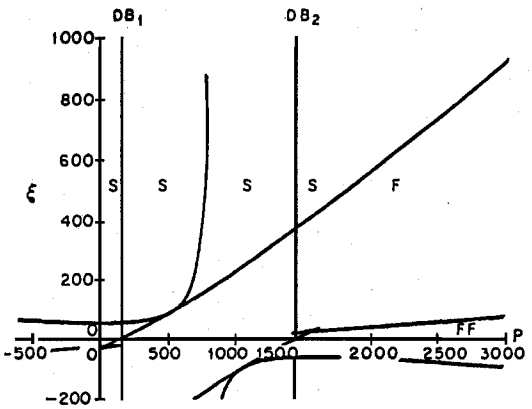

Fig. 4 Stability boundaries for the square beam with gyricity by a two-function approximation.

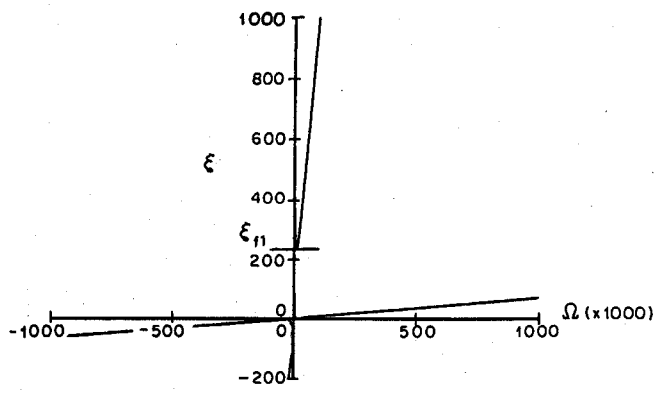

Fig. 6 Characteristic curves for the square beam with gyricity by a two-function approximation at $P = 1000$ N.

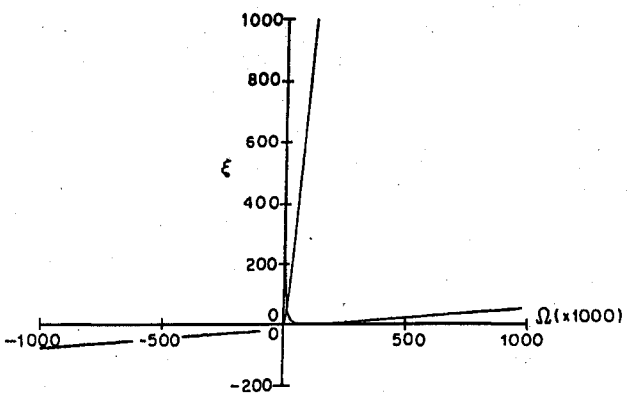

Fig. 5 Characteristic curves for the square beam with gyricity by a two-function approximation at $P = 0$ N.

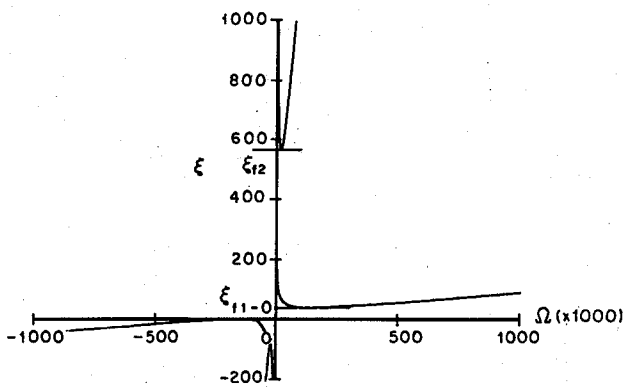

Fig. 7 Characteristic curves for the square beam with gyricity by a two-function approximation at $P = 2000$ N.

$$k_{12} = \int_0^L EI\phi_1'\phi_2' \, dz == \int_0^L EI\psi_1'\psi_2' \, dz = k_{34} \tag{60}$$

$$k_{22} = \int_0^L EI(\phi_2')^2 \, dz == \int_0^L EI(\psi_2')^2 \, dz = k_{44} \tag{61}$$

where (==) holds only if the beam has a square cross section.

When the numerical values from Table 1 are used, the divergence values are $P_{d_1} \simeq 142.7$ N and $P_{d_2} \simeq 1446$ N, where both are double roots. The exact values[22] for the divergence boundaries are given by $P_{d_1}^* \simeq 141.9$ N for the first boundary and by $P_{d_2}^* \simeq 1277$ N for the second boundary. The divergence and flutter boundaries in the P–ξ plane are plotted in Fig. 4, where the regions of stability, single flutter, and double flutter are indicated by S, F, and FF, respectively.

The characteristic curves in the frequency Ω–ξ plane for fixed values of the applied force P are plotted in Figs. 5–7. The no-load case ($P = 0$), which is representative of load values where $0 \leq P < P_{d_1}$, generates a characteristic curve (Fig. 5) with positive frequencies Ω for all values of ξ. Hence, in this load range, the system is stable regardless of the value of ξ. When the applied load values lies between the two divergence boundaries such that $P_{d_1} < P < P_{d_2}$ (at $P = 1000$ in Fig. 6), it is observed that there is a flutter critical value at $\xi = \xi_{f_1}$. With reference to Fig. 7, there is a critical point at $\xi = 0$ so that, for low values of ξ where $0 < \xi < \xi_{f_1}$, the frequencies consist of two positive values and a pair of complex values, resulting in an instability by single flutter which corresponds to region F in Fig. 4. The situation where $\xi = 0$ deserves special mention in that for this one value of ξ there is a single negative real root, a single positive real root, and a pair of complex roots, which makes this a point where divergence and flutter instabilities are present. As ξ increases through the threshold value (flutter value) $\xi = \xi_{f_1}$, and P is held constant at $P = 1000$, the system enters into a stable region where all of the roots are positive. This stability region exits because of the effect of the gyroscopic forces. The characteristic curves in Fig. 7 are for $P = 2000$, which places this value of P beyond the second divergence boundary ($P > P_{d_2}$). For this load, and others in this range of loading, it can be observed that there are flutter critical values at $\xi = 0$, $\xi = \xi_{f_1}$ and ξ_{f_2}. At $\xi = 0$, there is also a critical divergence point so that for $0 < \xi < \xi_{f_1}$ (i.e., for low values of ξ), the frequencies consist of two pairs of complex conjugates, indicating instability by double flutter (region FF in Fig. 4). At $\xi = 0$, there are a pair of negative real roots and a pair of complex roots, which means that the system possesses a double-divergence single-flutter instability behavior for this single value of ξ. Once ξ is increased past the first threshold value ξ_{f_1} and $\xi_{f_1} \leq \xi < \xi_{f_2}$, the frequencies consist of two positive values and a pair of complex conjugates, indicating instability by single flutter (region F in Fig. 4). When ξ takes on larger values where $\xi > \xi_{f_2}$, the system enters into a stable region with all-positive roots because of the effect of the gyroscopic forces. This is region S in Fig. 4.

3. *Example 3: Two-Function Approximation for a Rectangular Beam*

As the final example, the case of the rectangular beam using a two-function approximation is considered. The same parameter values as used in example 1 and given in Table 1 are used, and the characteristic equation $\Delta_2 = 0$ can be expressed in the same general form as Eq. (53) for the square beam, but with different specifics in the $\mathcal{P}_i$. In this case,

$$\mathcal{P}_4 = (m_{11}m_{22} - m_{12}^2)(m_{33}m_{44} - m_{34}^2) \tag{62}$$

which is always positive and depends only on the indicated entries in the mass matrix.

In this example, the values of P that correspond to the divergence boundaries satisfy $\mathcal{P}_0 = 0$, which leads to the following quartic equation in P:

$$\begin{aligned}
&(f_{11}f_{22} - f_{12}^2)(f_{33}f_{44} - f_{34}^2)P^4 \\
&\quad - [(f_{11}f_{22} - f_{12}^2)(f_{33}k_{44} + f_{44}k_{33} - 2f_{34}k_{34}) \\
&\quad + (f_{33}f_{44} - f_{34}^2)(f_{11}k_{22} + f_{22}k_{11} - 2f_{12}k_{12})]P^3 \\
&\quad + [(f_{11}f_{22} - f_{12}^2)(k_{33}k_{44} - k_{34}^2) + (f_{33}f_{44} - f_{34}^2)(k_{11}k_{22} - k_{12}^2) \\
&\quad + (f_{33}k_{44} + f_{44}k_{33} - 2f_{34}k_{34})(f_{11}k_{22} + f_{22}k_{11} - 2f_{12}k_{12})]P^2 \\
&\quad - [(k_{11}k_{22} - k_{12}^2)(k_{33}f_{44} + k_{44}f_{33} - 2f_{34}k_{34}) \\
&\quad + (k_{33}k_{44} - k_{34}^2)(k_{11}f_{22} - k_{22}f_{11} - 2f_{34}k_{34})]P \\
&\quad + (k_{33}k_{44} - k_{34}^2)(k_{11}k_{22} - k_{12}^2) = 0 \qquad (63)
\end{aligned}$$

where f_{ij}, k_{ij} are as given in Eqs. (56–61) and where (==) does not hold.

The divergence boundaries are given by four distinct vertical lines as

$$P_{d_1} \simeq 285.4\,\text{N}, \qquad P_{d_2} \simeq 1142\,\text{N} \qquad (64)$$

$$P_{d_3} \simeq 2891\,\text{N} \quad \text{and} \quad P_{d_4} \simeq 11{,}560\,\text{N} \qquad (65)$$

The first two exact values for the divergence boundaries are as given in example 1, and the next two are $P_{d_3}^* \simeq 2554$ N and $P_{d_4}^* \simeq 10{,}220$ N (Ref. 22). The divergence and flutter boundaries in the P–ξ plane are plotted in Fig. 8, where it is evident that this example is more complicated than any of those previously considered.

Rather than examining the characteristic curves for this example (these can be found in Yamanaka[19]), it is more interesting to consider a horizontal ray in Fig. 9 at $\xi = 700$ that results in the

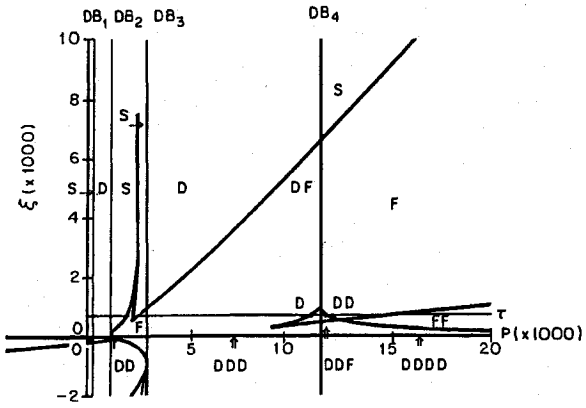

Fig. 8 Stability boundaries for the rectangular beam with gyricity by a two-function approximation.

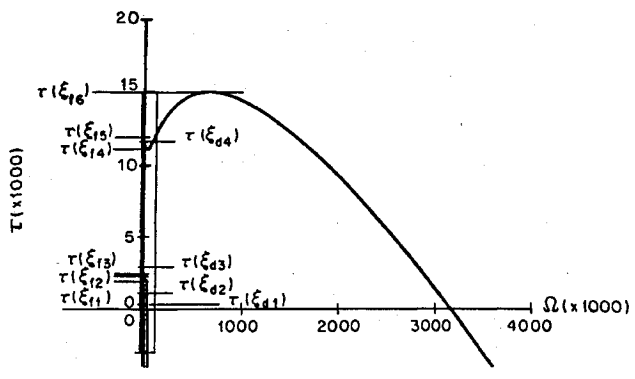

Fig. 9 Frequency distance, Ω, along a horizontal ray τ at $\xi = 700$ for the rectangular beam by a two-function approximation.

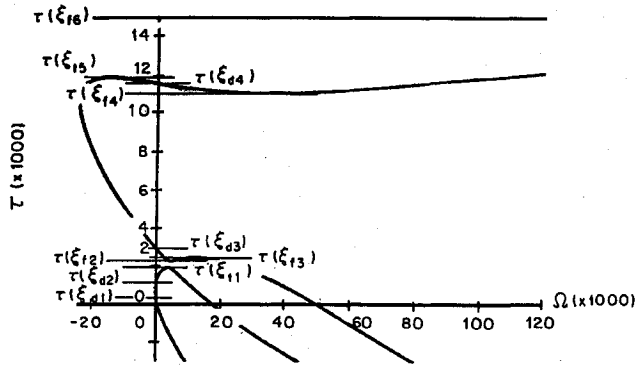

Fig. 10 Enlarged part of Fig. 9.

curves in Figs. 9 and 10, where the ray length τ is equivalent to the external force P. In these figures, it can be observed that for $0 \le \tau(\xi) < \tau(\xi_{d_1})$ [i.e., for values of $\tau(\xi)$ that are below the first divergence load value], all of the frequencies are positive, indicating stability in region S in Fig. 8. At $\tau(\xi) = \tau(\xi_{d_1})$, there is a critical divergence point because this value of τ corresponds to the first divergence boundary DB_1 in Fig. 8. When the value of τ places the point of interest between the first and the second divergence boundary $[\tau(\xi_{d_1}) < \tau(\xi) < \tau(\xi_{d_2})]$, the frequencies consist of one negative value and three positive values, indicating that in this region there is instability by single divergence (region D in Fig. 8). There is a critical divergence point at the second divergence boundary DB_2 when $\tau(\xi) = \tau(\xi_{d_2})$ in Fig. 9. For $\tau(\xi_{d_2}) < \tau(\xi) \le \tau(\xi_{f_1})$, all of the frequencies consist of positive values, indicating stability in the region to the right of the second divergence boundary DB_2 (Fig. 8) that is marked with an S. Still with reference to Figs. 9 and 10, it can be seen that when $\tau(\xi_{f_1}) < \tau(\xi) < \tau(\xi_{f_2})$, the frequencies consist of two positive values and a pair of complex conjugates, indicating that this range of values of τ lies in a region of instability by single flutter. In Fig. 8, this is the small region that is marked F between the second and third divergence boundaries. Further increases in the value of τ, so that $\tau(\xi_{f_2}) \le \tau(\xi) \le \tau(\xi_{f_3})$, places us again in a stable region in the ξ–P plane region where all of the frequencies consist of positive values. This region lies immediately to the left of the third divergence boundary DB_3 in Fig. 8. Thus, for values of ξ that correspond to this ray, there are three regions of stability that are separated by regions of instability. Further examination of Figs. 9 and 10 show that there are no more stability regions for this particular value of ξ, but reference to Fig. 8 readily illustrates that there are other values of ξ at which similar behavior is indicated. For $\tau(\xi_{f_3}) < \tau(\xi) < \tau(\xi_{d_3})$, the frequencies consist of two positive values and a pair of complex conjugates, indicating instability by single flutter in the region marked F to the left of DB_3 in Fig. 8. At $\tau(\xi) = \tau(\xi_{d_3})$, there is another critical divergence point that corresponds to the third divergence boundary DB_3 in Fig. 8. When the values of τ satisfy $\tau(\xi_{d_3}) < \tau(\xi) < \tau(\xi_{f_4})$, the frequencies consist of one negative value, one positive value, and a pair of complex conjugates, indicating instability by single divergence and single flutter. This region, DF in Fig. 8, exists over a relatively wide range of values of the load P. We find a small region of single divergence, region D in Fig. 8, near the fourth divergence boundary DB_4. This region occurs on the interval $\tau(\xi_{f_4}) \le \tau(\xi) < \tau(\xi_{d_4})$, and here the frequencies consist of one negative value and three positive values. The last critical divergence point occurs at $\tau(\xi) = \tau(\xi_{d_4})$ and is the divergence boundary DB_4 in Fig. 8. Just to the right of DB_4, where $\tau(\xi_{d_4}) < \tau(\xi) \le \tau(\xi_{f_5})$, it is found that the frequencies consist of two negative values and two positive values, indicating that, in this small region, there is instability by double divergence (region DD in Fig. 8). For $\tau(\xi_{f_5}) < \tau(\xi) \le \tau(\xi_{f_6})$, the frequencies consist of two positive values and a pair of complex conjugates, which makes this a region of instability by single flutter (region F in Fig. 8). There are no further boundary curves that can be encountered when $\tau(\xi) > \tau(\xi_{f_6})$, and for these very large values of P, the frequencies consist of two pairs of complex conjugates, indicating instability by double flutter. This is region FF along the ray to the far right in Fig. 8.

Observe in Figs. 9 and 10 how one of the Ω-τ curves decreases between $\tau(\xi_{f5})$ and $\tau(\xi_{f4})$ from a negative-frequency region to a positive-frequency region. It is because of the decreasing values of the curve that regions D and DD around the fourth divergence boundary DB_4 in Fig. 8 are generated.

IV. Two-Function Characteristic Curves

To better understand the stability behavior of the two-function approximation of the beam (examples 2 and 3), let us focus on the general expression for the characteristic curves. It can be observed in Eq. (53) that Δ_2 is quadratic in ξ, and therefore (53) can be written as

$$\xi_{1,2} = (1/\Omega)[\mathcal{A}_2(a,P)\Omega^2 + \mathcal{A}_1(a,P)\Omega + \mathcal{A}_0(a,P) \pm \sqrt{\mathcal{B}_4(a,P)\Omega^4 + \mathcal{B}_3(a,P)\Omega^3 + \mathcal{B}_2(a,P)\Omega^2 + \mathcal{B}_1(a,P)\Omega + \mathcal{B}_0(a,P)} \tag{66}$$

where the coefficients $\mathcal{A}_i$ and $\mathcal{B}_j$ are polynomial, but not necessarily linear, in the external force P. The parameter ξ is the square of the angular momentum of the gyricity, and the length of the cross section of the rectangular beam in the Y direction is fixed at 1 cm, whereas the length in the X direction is denoted by a. From Eq. (66) it can be observed that the vertical line $\Omega = 0$ in the Ω–ξ plane is, in general, an asymptote and that the characteristic curves $\xi_{1,2}$ in Eq. (66) never cross each other in accordance with the observation made by D'Eleuterio.[12] The argument of the radical can be expressed as

$$\mathcal{B}_4\Omega^4 + \mathcal{B}_3\Omega^3 + \mathcal{B}_2\Omega^2 + \mathcal{B}_1\Omega + \mathcal{B}_0 = \mathcal{B}_4(\Omega - C_1)(\Omega - C_2)(\Omega - C_3)(\Omega - C_4) = \Delta_R \tag{67}$$

and because, in general, $\mathcal{B}_4 > 0$, it is apparent that

$$\mathcal{B}_0/\mathcal{B}_4 = C_1C_2C_3C_4 \tag{68}$$

If the interval of frequencies $[\Omega]$, corresponding to the values of Ω that result in $\Delta_R < 0$, span from the negative-frequency region to the positive-frequency region, then at least one root C_i will be negative real and at least one root C_j will be positive real. Therefore, the boundary where the condition that one root of $\Delta_R = 0$ is negative and another is positive is given by

$$\mathcal{B}_0 = 0 \tag{69}$$

Let us focus on the coefficients of the characteristic equation $\Delta = 0$ of the general expression as in examples 1 and 3. The general expression for the characteristic equation $\Delta = 0$ for a two-function approximation can be expressed as

$$\Delta = \mathcal{P}_4\Omega^4 + \mathcal{P}_3\Omega^3 + \mathcal{P}_2\Omega^2 + \mathcal{P}_1\Omega + \mathcal{P}_0 = 0 \tag{70}$$

Because, in general, $\mathcal{P}_4 > 0$, the above equation can be expressed as

$$\Delta = \mathcal{P}_4(\Omega^4 + \mathcal{Q}_3\Omega^3 + \mathcal{Q}_2\Omega^2 + \mathcal{Q}_1\Omega + \mathcal{Q}_0) = 0 \tag{71}$$

or, alternatively, Δ can be expressed in factored form as

$$\Delta = \mathcal{P}_4(\Omega - \Omega_1)(\Omega - \Omega_2)(\Omega - \Omega_3)(\Omega - \Omega_4) = 0 \tag{72}$$

The coefficients $\mathcal{Q}_i$ can be expressed in terms of the roots Ω_i as

$$\mathcal{Q}_3 = -(\Omega_1 + \Omega_2 + \Omega_3 + \Omega_4) \tag{73}$$

$$\mathcal{Q}_2 = \Omega_1\Omega_2 + \Omega_1\Omega_3 + \Omega_1\Omega_4 + \Omega_2\Omega_3 + \Omega_2\Omega_4 + \Omega_3\Omega_4 \tag{74}$$

$$\mathcal{Q}_1 = -(\Omega_1\Omega_2\Omega_3 + \Omega_1\Omega_2\Omega_4 + \Omega_1\Omega_3\Omega_4 + \Omega_2\Omega_3\Omega_4) \tag{75}$$

and

$$\mathcal{Q}_0 = \Omega_1\Omega_2\Omega_3\Omega_4 \tag{76}$$

Because all of the frequencies Ω_i ($i = 1, 2, 3, 4$) must be real and positive for the system to be stable, the following necessary conditions can be applied as the positive root condition:

i) $\mathcal{Q}_3 < 0 \Rightarrow \mathcal{B}_3 - 2\mathcal{A}_2(\mathcal{A}_1 - \xi) > 0$

ii) $\mathcal{Q}_2 > 0 \Rightarrow 2\mathcal{A}_2\mathcal{A}_0 + (\mathcal{A}_1 - \xi)^2 - \mathcal{B}_2 > 0$

iii) $\mathcal{Q}_1 < 0 \Rightarrow \mathcal{B}_1 - 2(\mathcal{A}_1 - \xi) > 0$

iv) $\mathcal{Q}_0 > 0 \Rightarrow \mathcal{A}_0^2 - \mathcal{B}_0 > 0$ (77)

The form of the condition in the right-hand column of Eq. (77) is in terms of the coefficients in Eq. (66). Considering condition (iv), if the values of $\mathcal{B}_0$ are positive, this condition can be expressed as

$$(\mathcal{A}_0 - \sqrt{\mathcal{B}_0})(\mathcal{A}_0 + \sqrt{\mathcal{B}_0}) > 0 \tag{78}$$

Condition (iv) also is related to the divergence boundaries, which satisfy $\mathcal{A}_0 \pm \sqrt{(\mathcal{B}_0)} = 0$. In this form, Eq. (78) indicates that cases where $\mathcal{B}_0 < 0$ correspond to physically unrealizable values of the angular momentum ξ. Therefore, as long as the system is outside of the unreachable region, $\mathcal{B}_0 > 0$ is guaranteed. The divergence boundaries can be expressed by the following four equations:

$$db_1 = 143a, \qquad db_2 = 143a^3$$
$$db_3 = 1446a, \qquad db_4 = 1446a^3 \tag{79}$$

The boundaries, in the a–P plane, corresponding to $\mathcal{B}_0 = 0$ and to the divergence boundaries db_1, db_2, db_3, and db_4, are plotted in Fig. 11, where it can be observed that at $a = 1 = db_1 = db_2$ and $db_3 = db_4$, which corresponds to the two pairs of divergence values encountered in the square-beam example. For cases where $a < 1$, $db_2 < db_1$, and $db_4 < db_3$, which occurs because, by having $a < 1$, the direction that corresponds to the direction of least bending stiffness is the same as the direction with the greatest bending stiffness for $a > 1$.

Referring to example 2, the conditions for positive roots are plotted in Fig. 12, and stable regions are only possible in the areas indicated by arrows. The values of the load P that correspond to $\mathcal{B}_0 = 0$ can be calculated to be $P_{\mathcal{B}_{01}} = P_{\mathcal{B}_{02}} \simeq 794$. This value appears to correspond to the vertical asymptote of the spurious flutter boundary that lies between the first and second divergence boundaries in Fig. 12. Although this has been confirmed numerically, its analytical proof remains elusive.

Referring to the characteristic equation in example 3, the conditions for positive roots are plotted in Fig. 13, and stable regions are possible only in the areas indicated by arrows. From condition (iv) it can be deduced that stability cannot be obtained, regardless of the values of ξ, between the first and second divergence boundaries (DB_1 and DB_2) and between the third and fourth divergence boundaries (DB_3 and DB_4). The load values that satisfy $\mathcal{B}_0 = 0$ can be calculated approximately as $b_{\mathcal{B}_{01}} = b_{\mathcal{B}_{02}} \simeq 2541$. As in the case of the square beam, these values correspond numerically to the vertical asymptotes of the flutter boundaries that lie between the second and third divergence boundaries in Fig. 13.

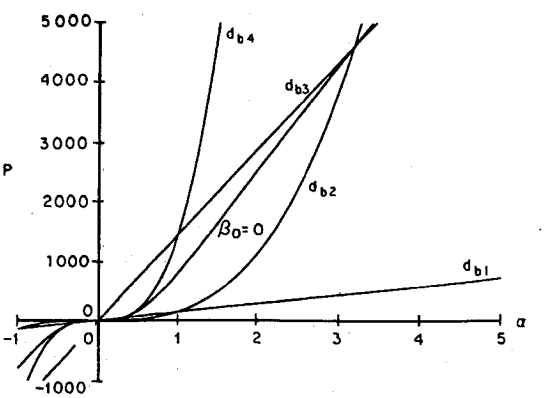

Fig. 11 Divergence boundaries and $\mathcal{B} = 0$ for the beam with gyricity.

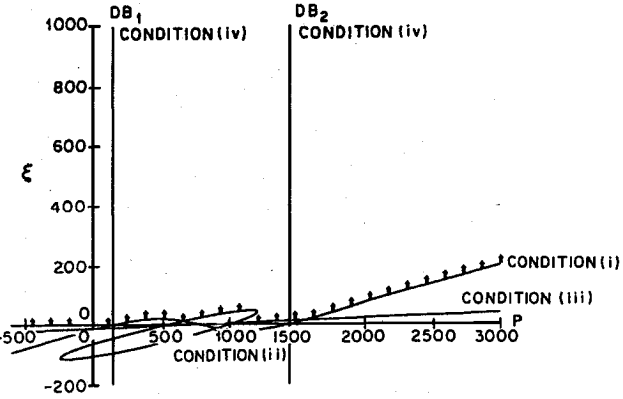

Fig. 12 Positive root conditions for the square beam with gyricity and with $a = b = 1$ cm.

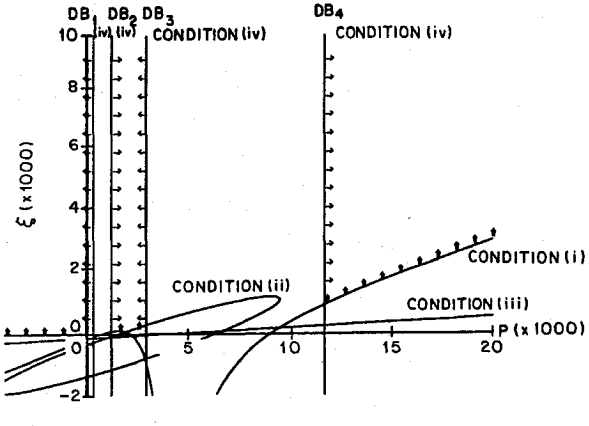

Fig. 13 Positive root conditions for the rectangular beam with gyricity and with $a = 1$ cm, $b = 2$ cm.

V. Conclusions

The governing equations of motion and the associated boundary conditions for a cantilever beam with a gyricity distribution have been derived. Application of the method of Ritz has allowed the determination of the stability behavior of the system where it has been shown that both divergence and flutter instabilities are possible and that secondary regions of stability can be present in the case of the rectangular beam.

References

[1]Meirovitch, L., "A New Method of Solution of the Eigenvalue Problem for Gyroscopic Systems," *AIAA Journal*, Vol. 12, No. 10, 1974, pp. 1337–1342.

[2]Huseyin, K., and Plaut, R. H., "Transverse Vibrations and Stability of Systems with Gyroscopic Forces," *Journal of Structural Mechanics*, Vol. 3, No. 2, 1974, pp. 163–177.

[3]Meirovitch, L., "A Modal Analysis for the Response of Linear Gyroscopic Systems," *Journal of Applied Mechanics*, Vol. 42, No. 2, 1975, pp. 446–450.

[4]Huseyin, K., "Standard Forms of the Eigenvalue Problems Associated with Gyroscopic Systems," *Journal of Sound and Vibration*, Vol. 45, No. 1, 1976, pp. 29–37.

[5]Huseyin, K., Hagedorn, P., and Teschner, W., "On the Stability of Linear Conservative Gyroscopic Systems," *ZAMP*, Vol. 34, No. 6, 1983, pp. 807–815.

[6]Inman, D. J., "A Sufficient Condition for the Stability of Conservative Gyroscopic Systems," *Journal of Applied Mechanics*, Vol. 55, No. 4, 1988, pp. 895–898.

[7]Huseyin, K., "On the Stability Criteria for Conservative Gyroscopic Systems," *Journal of Vibration and Acoustics*, Vol. 113, Jan. 1991, pp. 58–61.

[8]Kane, T. R., Likins, P. W., and Levinson, D. A., *Spacecraft Dynamics*, McGraw–Hill, New York, 1983, pp. 211–246.

[9]Hughes, P. C., *Spacecraft Attitude Dynamics*, Wiley, New York, 1986, pp. 65–83, 156–184.

[10]Wiesel, W. E., *Spaceflight Dynamics*, McGraw–Hill, New York, 1989, pp. 159–180.

[11]D'Eleuterio, G. M. T., and Hughes, P. C., "Dynamics of Gyroelastic Continua," *Journal of Applied Mechanics*,Vol. 51, No. 2, 1984, pp. 415–422.

[12]D'Eleuterio, G. M. T., "Dynamics of Gyroelastic Vehicles," Inst. for Aerospace Studies, Univ. of Toronto, UTIAS Rept. 300, Toronto, ON, Canada, 1986.

[13]D'Eleuterio, G. M. T., and Hughes, P. C., "Modal Parameter Analysis of Gyroelastic Continua," *Journal of Applied Mechanics*, Vol. 53, No. 4, 1986, pp. 918–924.

[14]D'Eleuterio, G. M. T., and Hughes, P. C., "Dynamics of Gyroelastic Spacecraft," *Journal of Guidance, Control, and Dynamics*, Vol. 10, No. 4, 1987, pp. 401–405.

[15]D'Eleuterio, G. M. T., "On the Theory of Gyroelasticity," *Journal of Applied Mechanics*, Vol. 55, No. 2, 1988, pp. 488, 489.

[16]Damaren, C. J., "An Optimal Control Formulation for Lightly Damped Gyroelastic Continua," M.A.Sc. Thesis, Univ. of Toronto, Toronto, ON, Canada, 1987.

[17]Damaren, D. C., "Optimal Control of Large Space Structures Using Distributed Gyricity: A Continuum Approach," Inst. for Aerospace Studies, Univ. of Toronto, UTIAS Rept. 341, Toronto, ON, Canada, 1990.

[18]Damaren, C. J., and D'Eleuterio, G. M. T., "Optimal Control of Large Space Structures Using Distributed Gyricity," *Journal of Guidance, Control, and Dynamics*, Vol. 12, No. 5, 1989, pp. 723–731.

[19]Yamanaka, K., "On the Stability of Gyroscopic Systems," Ph.D. Thesis, Dept. of Systems Design Engineering, Univ. of Waterloo, ON, Canada, 1993.

[20]Clough, R. W., and Penzien, J., *Dynamics of Structures*, McGraw–Hill, New York, 1975, pp. 312–314.

[21]Yamanaka, K., Heppler, G. R., and Huseyin, K., "On the Stability of Gyroscopic Systems," *Mathematical Modelling and Scientific Computing*, Vol. 2, 1993, pp. 438–443.

[22]Timoshenko, S. P., and Gere, J. M., *Theory of Elastic Stability*, McGraw–Hill, New York, 1961, pp. 46–49.